Experimental insights into Stannern-trend eucrite petrogenesis

S. D. CROSSLEY[1,2], N. G. LUNNING [iD][3*], R. G. MAYNE[1], T. J. McCOY [iD][3], S. YANG[4],
M. HUMAYUN[4], R. D. ASH[2], J. M. SUNSHINE[5], R. C. GREENWOOD[6], and I. A. FRANCHI[6]

[1]Monnig Meteorite Collection, Texas Christian University, TCU Box 298830, Fort Worth, Texas 76109, USA
[2]Department of Geology, University of Maryland, College Park, Maryland 20742, USA
[3]Department of Mineral Sciences, Smithsonian Institution, National Museum of Natural History, Washington, DC 20560, USA
[4]National High Magnetic Field Laboratory and Department of Earth, Ocean & Atmospheric Science, Florida State University,
Tallahassee, Florida 32310, USA
[5]Department of Astronomy, University of Maryland, College Park, Maryland 20742, USA
[6]Planetary and Space Sciences, School of Physical Sciences, The Open University, Walton Hall, Milton Keynes MK7 6AA, UK
*Corresponding author. E-mail: lunningn@si.edu

Abstract–The incompatible trace element-enriched Stannern-trend eucrites have long been recognized as requiring a distinct petrogenesis from the Main Group-Nuevo Laredo (MGNL) eucrites. Barrat et al. (2007) proposed that Stannern-trend eucrites formed via assimilation of crustal partial melts by a MGNL-trend magma. Previous experimental studies of low-degree partial melting of eucrites did not produce sufficiently large melt pools for both major and trace element analyses. Low-degree partial melts produced near the solidus are potentially the best analog to the assimilated crustal melts. We partially melted the unbrecciated, unequilibrated MGNL-trend eucrite NWA 8562 in a 1 atm gas-mixing furnace, at IW-0.5, and at temperatures between 1050 and 1200 °C. We found that low-degree partial melts formed at 1050 °C are incompatible trace element enriched, although the experimental melts did not reach equilibrium at all temperatures. Using our experimental melt compositions and binary mixing modeling, the FeO/MgO trend of the resultant magmas coincides with the range of known Stannern-trend eucrites when a primary magma is contaminated by crustal partial melts. When experimental major element compositions for eucritic crustal partial melts are combined with trace element concentrations determined by previous modeling (Barrat et al. 2007), the Stannern-trend can be replicated with respect to both major, minor, and trace element concentrations.

INTRODUCTION

The howardites, eucrites, and diogenites (HEDs) are a clan of meteorites that originate from a common parent body, thought to be the asteroid (4) Vesta (e.g., McCord et al. 1970; McSween et al. 2013). Howardites are breccias formed by mixing on or near the surface of the HED parent body. These breccias include clasts of both diogenitic and eucritic material (Duke and Silver 1967; Beck et al. 2012; Lunning et al. 2016a), and may include additional noneucritic or nondiogenitic materials (Gounelle et al. 2003; Barrat et al. 2012; Lunning et al. 2015, 2016b; Hahn et al. 2017). The diogenites are orthopyroxenites and harzburgites that formed in

crustal intrusions and/or the mantle of the HED parent body (Barrat et al. 2008; Beck and McSween 2010; Shearer et al. 2010). The eucrites are basalts and gabbros, which predominantly formed the primary crust of the HED parent body. Eucrites are typically characterized by their primary igneous history; however, most eucrites also record secondary brecciation, other shock features from impacts, thermal metamorphism, and/or metasomatism (Delaney et al. 1983; Takeda and Graham 1991; Yamaguchi et al. 1996, 1997; Barrat et al. 2011; Zhang et al. 2013).

The eucrites are divided into three subgroups: cumulate, noncumulate, and residual (e.g., Mittlefehldt and Lindstrom 1993; Yamaguchi et al. 2009). The cumulate

eucrites are defined by evidence of crystal accumulation, and typically lower concentrations of incompatible elements coupled with positive Eu anomalies associated with plagioclase accumulation. The noncumulate eucrites are further subdivided into the Main Group-Nuevo Laredo (MGNL) trend and the Stannern-trend (Warren and Jerde 1987). Compared to MGNL eucrites, Stannern-trend eucrites can be distinguished by higher concentrations of La and Ti relative to Mg (and/or Fe), as well as higher concentrations of La and Hf relative to Sc (Stolper 1977; Mittlefehldt and Lindstrom 2003; Mittlefehldt 2015). The residual eucrites are distinguished by light rare earth element (REE) depletions and positive Eu anomalies indicating that they underwent low degrees of partial remelting, with the resulting melt being extracted from the residual parent eucrite (Yamaguchi et al. 2009). Stolper (1977) experimentally established that MGNL-trend eucrites could be explained as a single magmatic suite that experienced varying degrees of fractional crystallization. The MGNL-trend includes rocks, such as Juvinas, that represent the primary magmas of this suite, to more evolved Fe-rich and incompatible element-rich rocks, such as Nuevo Laredo, that formed after their primary magmas were modified by fractional crystallization. In contrast, Stannern-trend eucrites cannot be explained by fractional crystallization of Juvinas-composition primary magmas (e.g., Stolper 1977; Warren and Jerde 1987; Mittlefehldt and Lindstrom 2003). Instead, it has been proposed that they could have originated from a different parent body (Mittlefehldt and Lindstrom 2003), or that they may have crystallized in situ within a magma ocean (Barrat et al. 2000). However, these models are not widely considered to represent viable mechanisms for Stannern-trend formation.

Barrat et al. (2007) modeled the petrogenesis of Stannern-trend eucrites by a process of assimilation involving the mixing of a MGNL eucritic magma with low-degree crustal partial melts removed from eucrites (subsequently described as the residual eucrites by Yamaguchi et al. 2009). The model of Barrat et al. (2007) accounts for the incompatible trace element enrichments of the Stannern-trend, as well as significant negative Eu, Ba, and Sr anomalies. This model does not address whether major element chemistry, which is similar between MGNL eucrites and Stannern-trend eucrites, can be accommodated within an assimilation model. This is equally important if this model is viable. However, it is difficult to coincidently model trace and major element trends even in well-understood terrestrial systems (e.g., Hanson and Langmuir 1978).

Petrologic experiments provide a potential way to investigate both major and trace element compositions that can be directly measured in the resulting melts. Stolper (1977) measured major and minor (e.g., Ti, Cr)

elements, but not trace elements that would prove essential to investigating the formation process for Stannern-trend eucrites. Yamaguchi et al. (2013) focused on trace element analyses in their partial melting experiments of eucrites. Yamaguchi et al. (2013) partially melted the Main Group (MG) eucrite Hammadah al Hamra 262 (HaH 262) at an oxygen fugacity (fO_2) of iron-wüstite (IW)-1, and temperatures of 1050, 1070, and 1100 °C. They were only able to measure the trace element concentrations in the 1100 °C experiments, as the melt products generated at lower temperatures were too small for direct compositional analysis. Additionally, Yamaguchi et al. (2013) reported a few experimental artifacts (Fe-loss to Pt foil container and quench crystallization of pyroxene and Fe-rich olivine) that may have modified the major element concentrations in the melt products, while having a relatively smaller influence on the incompatible trace element concentrations. Stolper (1977) partially melted a broad range of eucrites and analyzed the major and minor element concentrations in melt products from these experiments. At oxygen fugacities below the iron-wüstite buffer, IW-0.6, 1108 °C is the lowest temperature that Stolper (1977) reported compositions of partial melts of MGNL eucrites. Yamaguchi et al. (2013) and Stolper (1977) observed melting in their charges for experiments at temperatures as low as 1050 and ~1060 °C, respectively. In the Yamaguchi et al. (2013) experiments, these melts were not analyzed because they were not spatially large enough. One of the primary goals in the selection of our experimental sample material was to generate melt pools large enough to analyze. Thus, the sample for this study was chosen to extend the experimental work done by Yamaguchi et al. (2013) on the equilibrated MG eucrite HaH 262. The two petrologic characteristics that will particularly increase the percentage of melt generated include (1) a smaller grain size because melting initiates along grain boundaries, and rocks with smaller grain sizes have a greater volume of grain boundaries relative to overall volume; and (2) a more FeO-rich MG eucrite will generate a greater volume of melt at a given temperature. As demonstrated by Stolper (1977), Mg-rich Main Group (MG) eucrites, like HaH 262, and more Fe-rich MG eucrites, such as the eucrite used in this study, will yield low-temperature partial melts of the same composition; Mg-rich eucrites will just yield a lower modal abundance of those melts.

Here, we examine the Barrat et al. (2007) assimilation model for the petrogenesis of the Stannern-trend by experimentally generating low-degree partial melt pools of sufficient size for major and trace element analysis. We chose experimental procedures to maximize the melt preserved in our charges, as will be described in the following section. Our experiments utilize a fine-grained

and slightly FeO-rich MG eucrite, Northwest Africa 8562 (NWA 8562), which we petrologically characterized as part of this work. Subsequently, we model the major and trace element composition of magmas formed by assimilation of low percentages (5–15%) of our experimental partial melt products into MGNL-trend composition magmas, as well as combining our experimental data with the results from the trace element modeling of Barrat et al. (2007).

METHODS

Chips and two polished thin sections of the eucrite NWA 8562 were allocated from the Monnig Meteorite Collection at Texas Christian University for experimental and destructive analyses.

Experimental Methods

All our experiments were run at 1 atm (=0.101 MPa = 1.01 bar) pressure in a Deltech vertical tube furnace at the Smithsonian Institution (SI). Five experiments were run at a fO_2 of IW-0.5 at temperatures of 1050, 1075, 1100, 1150, and 1200 °C. In each experiment, a chip (290–441 mg) of NWA 8562 was heated inside an alumina crucible at the target temperature and fO_2. An alumina crucible was used because Fe is not lost from experimental charges to this container. One experiment was run for 48 h (the 1075 °C experiment) and the other four experiments were run for 24 h, similar to run times for the experiments of Stolper (1977) and Yamaguchi et al. (2013).

Temperatures were set with a type B thermocouple ($Pt_{70}Rh_{30}$-$Pt_{94}Rh_6$) in the hanging assembly with the experimental charge, facilitating temperature measurement and regulation during the experiments. Prior to each set of experiments, the thermocouple was calibrated against the melting point of Au (T_{melt} = 1064 °C). The thermocouple has a resolution of 1 °C and an accuracy of ±5 °C. Oxygen fugacity was also monitored and regulated during our experiments using an yttrium-doped zirconia assembly with one side exposed to the furnace gas mixture and with pure O_2 reference gas flowing to the other side. Prior to each set of experiments, the fO_2 sensor was calibrated against a premixed reference gas with a fixed $CO:CO_2$ ratio. The fO_2 sensor had an accuracy of ±0.2 log units. During our experiments, the fO_2 was held constant with a $CO+CO_2$ gas mixture. Experiments were drop-quenched in situ into water after 24 or 48 h. The method of drop-quenching into water was included to increase the preservation of melt in the lowest temperature experiments, as Yamaguchi et al. (2013) reported features potentially associated with some crystallization of pyroxene and Fe-rich olivine during air quenching. Crystallization of pyroxene and olivine during quenching

may not dramatically change the incompatible trace element composition of the melt, but could potentially modify the major element melt composition by incorporation of FeO and MgO in olivine and pyroxene.

The lowest run temperatures (1050 and 1075 °C) were chosen based on previous estimates of the solidus for noncumulate eucrites. Yamaguchi et al. (2013) reported very low degrees of partial melting of the eucrite HaH 262 at 1050 °C. Stolper (1977) reported that melt could not be positively identified at and/or only trace amounts of melting occurred in experiments on the eucrites Juvinas and Sioux County at 1060 °C.

Analytical Methods

Petrographic observations of the starting material were made at Texas Christian University and the SI. Backscattered electron (BSE) images and energy dispersive X-ray spectrometer (EDS) maps of the two polished sections of the unheated NWA 8562 were collected with the FEI Nova NanoSEM 600 at the SI. BSE images of all five experimental charges were also collected. Whole-charge (or thin section for unheated) BSE mosaics were overlain with a grid to assist systematic point counting to determine melt and mineral modal abundances.

In Situ Major and Minor Element Analyses

Major and minor element concentrations in glass and/or silicate mineral phases in the experimental charges for 1050, 1100, 1150, and 1200 °C experiments and the unheated NWA 8562 material were analyzed at the University of Oklahoma (OU) with the Cameca SX-100 electron microprobe (EMP). Glass was analyzed at 20 kV and 20 nA with 20 μm diameter spots. Detection limits (wt%) for glass analyses were SiO_2 0.11, TiO_2 0.01, Al_2O_3 0.07, Cr_2O_3 0.03, FeO 0.03, NiO 0.03, MnO 0.05, MgO 0.02, CaO 0.04, Na_2O 0.16, K_2O 0.06, and P_2O_5 0.02. Silicate minerals were analyzed at 20 kV and 20 nA with 2 μm diameter spots. Detection limits for silicate mineral analyses (wt%) were SiO_2 0.03, TiO_2 0.01, Al_2O_3 0.02, Cr_2O_3 0.02, FeO 0.03, NiO 0.03, MnO 0.01, MgO 0.03, CaO 0.01, Na_2O 0.03, K_2O 0.01, and P_2O_5 0.02. Analyses of secondary natural standards were conducted, and ±1% of standard values was maintained.

Glass, plagioclase, and pyroxene major and minor element compositions in the 1075 °C experiment were analyzed at SI with the JEOL 8900R EMP. Glass and plagioclase were at 15 kV and 20 nA with 5 μm diameter spots. Detection limits (wt%) for glass and plagioclase analyses were SiO_2 0.04, TiO_2 0.05, Al_2O_3 0.04, Cr_2O_3 0.04, FeO 0.09, NiO 0.07, MnO 0.11, MgO 0.04, CaO 0.02, Na_2O 0.08, K_2O 0.01, and P_2O_5 0.20. Pyroxene was analyzed at 15 kV and 30 nA with 1 μm

diameter spots. Detection limits for pyroxene analyses in wt% were SiO_2 0.03, TiO_2 0.04, Al_2O_3 0.03, Cr_2O_3 0.03, FeO 0.07, NiO 0.05, MnO 0.08, MgO 0.03, CaO 0.02, Na_2O 0.05, K_2O 0.01, and P_2O_5 0.20. Analyses of secondary natural standards were conducted and $\pm2\%$ or better consistency with these standards' known composition was maintained for all elements, except for Na using the pyroxene analysis conditions which exhibited as high as 10 wt% deviations from standard compositions.

EMP data presented here are averages of phases for each experiment with appropriate totals (99–101% for minerals and 97–101% for glasses). Natural and synthetic standards were used for EMPA calibration at both OU and SI.

In Situ Trace Element Analyses

All in situ major and trace element data for the unheated NWA 8562 material and the 1100, 1150, and 1200 °C experimental charges were collected using an ESI™ UP193FX ArF excimer laser coupled to a Thermo Element XR™ high-resolution inductively coupled plasma–mass spectrometer (LA-ICP-MS) at Florida State University (FSU) (Yang et al. 2015; Oulton et al. 2016). Bulk analyses of the starting material were conducted using a 75 μm spot rastered at 10 μm s^{-1} with 50 Hz laser repetition rate over an area of 1.1×0.7 mm on thick section NWA 8562_1 following established methods (Yang et al. 2015). Spot sizes of the analyses were 25–50 μm for silicates (i.e., pyroxene and plagioclase) in the unheated sample, with 50 Hz laser repetition rate and 10 s of laser dwell time. Three USGS glass standards were used for calibration purposes: BHVO-2g, BCR-2g, and BIR-1g. The precision of the major element analyses is ~2% (Humayun et al. 2010). For trace elements and REE, the precision is better than 2–5% for analyses with concentrations ≥1 ppm (Oulton et al. 2016). Information on peaks analyzed, typical detection limits, etc., are given elsewhere (Yang et al. 2015).

All in situ trace element data for the 1075 and 1050 °C experiments were measured using a ThermoFinnigan Element 2 inductively coupled plasma–mass spectrometer (ICPMS), coupled to a New Wave UP213 ultraviolet laser ablation system at the University of Maryland Plasma Mass Spectrometry Laboratory. Samples were ablated into a stream of helium (approximately 0.6 L min^{-1}), which was then mixed with Ar (approximately 0.9 L min^{-1}) before introduction into the mass spectrometer. Laser ablation was by spot analyses using a spot size varying from 15 to 55 μm, depending on the size of the grain to be ablated. The output of the laser was modified to ensure the flux remained between 2 and 4 J cm^{-2}, typically an output of approximately 60% of the total available power. The repetition rate of the laser was 7 Hz. Samples were

standardized using the NIST 610 alumino-silicate glass standard with results compared to USGS BHVO-2g and BCR-2g basaltic reference materials used as control standards when measuring the entire range of trace elements. Standards were analyzed in identical fashion to their respective samples. All samples were cleaned with a brief, low power pulse of the laser prior to the data gathering ablation. Gas background measurements were taken for 20 s prior to sample analysis. LAMTRACE was used for data reduction. Upper limits for concentration were calculated by setting the detection limit for any given isotope measured as three times the mean measured gas background. The uncertainties for trace element concentrations of the average 1075 °C experimental melt are the standard deviation (1σ) of the four melt pools analyzed, which are 0.935 ppm for La and 2.42 ppm for Sc. Analytical uncertainties (1σ) for La (1.77 ppm) and Sc (6.79 ppm) in the melt of the 1050 °C experiment are calculated by Poisson counting statistics for the single analysis.

Melt fraction was calculated from the concentration of REE and the highly incompatible elements Th, Ta, and Hf using the simplified batch melting equation $C_L/C_0 = 1/F$, where C_L is the concentration of the element in the glass, C_0 is the concentration in the bulk, and F is the melt fraction.

Whole-Rock Oxygen Isotope Analysis

An approximately 2 g chip of NWA 8562 was powdered and homogenized. Two aliquots of this powder, each with an approximate weight of 2 mg, were then loaded for oxygen isotope analysis at the Open University, using an infrared laser-assisted fluorination system (Miller et al. 1999). The powders were heated in the presence of BrF_5. After fluorination, the released oxygen gas was purified by passing it through two cryogenic nitrogen traps and over a bed of heated KBr. Oxygen gas was analyzed using a MAT 253 dual inlet mass spectrometer. System precision, as defined by replicate analyses ($n = 39$) of our internal obsidian standard, is: $\pm0.05‰$ for $\delta^{17}O$, $\pm0.09‰$ for $\delta^{18}O$, and $\pm0.02‰$ for $\Delta^{17}O$ (2σ).

Oxygen isotopic analyses are reported in standard δ notation, where $\delta^{18}O$ has been calculated as: $\delta^{18}O = ([^{18}O/^{16}O]_{sample}/[^{18}O/^{16}O]_{ref} - 1) \times 1000$ (‰) and similarly for $\delta^{17}O$ using the $^{17}O/^{16}O$ ratio, the reference being VSMOW: Vienna Standard Mean Ocean Water. $\Delta^{17}O$, which represents the deviation from the terrestrial fractionation line, has been calculated using the linearized format of Miller (2002):

$$\Delta^{17}O = 1000 \ln(1 + \delta^{17}O/1000) - \lambda\, 1000 \ln(1 + \delta^{18}O/1000)$$
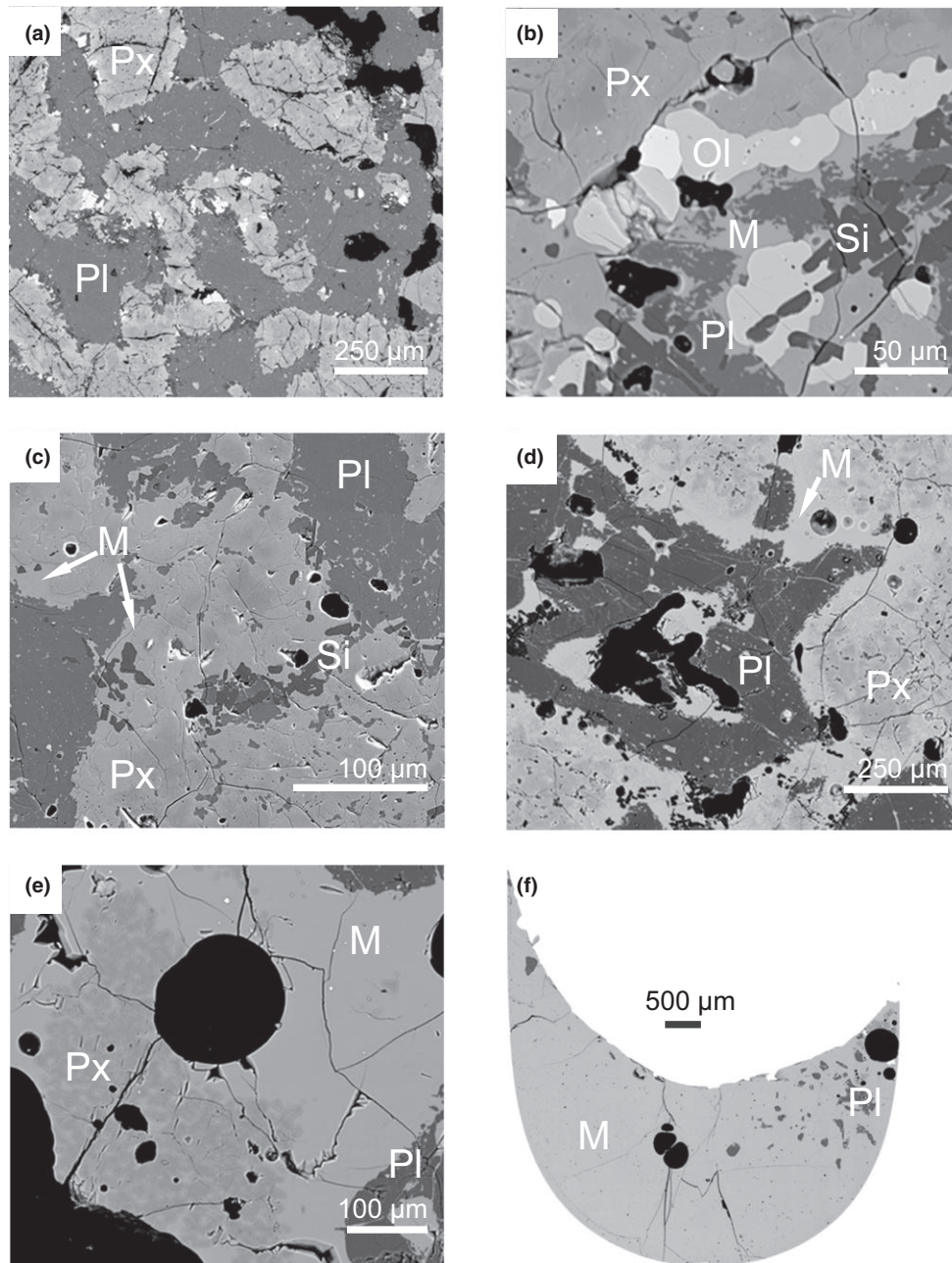
Fig. 1. BSE images of NWA 8562 and experimental products. (a) Unheated NWA 8562, (b) 1050 °C, (c) 1075 °C, (d) 1100 °C, (e) 1150 °C, and (f) 1200 °C. Phases are labeled as M = melt, Px = pyroxene, Pl = plagioclase, Ol = olivine, and Si = silica.

where $\lambda = 0.5247$, which was determined using 47 terrestrial whole-rock and mineral-separate samples (Miller et al. 1999; Miller 2002).

RESULTS

Characterization of Starting Material

NWA 8562 has a subophitic texture and is relatively fine-grained (Fig. 1a). Pyroxene grains are typically hundreds of μm in their longest dimensions with the largest pyroxene grains <1.2 mm. Plagioclase grains are also typically only hundreds of μm in their longest dimensions with the largest phenocrysts ≤2.2 mm long. Plagioclase–pyroxene grain boundaries are highly irregular and intergrown, with embayments of each phase into the other on scale of a few to tens of μm. Plagioclase commonly contains small inclusions of troilite (generally <2 μm in diameter). Individual pyroxene grains exhibit undulatory extinction with

planar deformation features with edges of grains or, in some cases entire grains, grading to mosaicism, a shock-induced feature in which larger crystals exhibit domains with differing extinction on the scale of a few μm in response to impact (e.g., Bischoff and Stöffler 1992). Silica laths (1–150 μm) and olivine also occur outside of mesostasis areas, often intergrown with rims of both pyroxene and plagioclase. Olivine (usually <100 μm) often occurs with chromite, ilmenite, troilite, spinel, and silica. Ca-rich phosphates (1–2 μm) were identified in thin section by EDS analysis, but are too small for EMP analysis. The phosphates occur in mesostasis areas and plagioclase rims in association with silica laths and/or similarly sized Fe-sulfide grains. Chromite forms the largest oxides (up to 200 μm), but tends to be less abundant than ilmenite and ülvospinel, which are smaller (<5 and 50 μm, respectively), and often occur as inclusions in chromite.

NWA 8562 is dominated by pyroxene and plagioclase in roughly equal proportions, typical of both monomict and unbrecciated eucrites (Duke and Silver 1967; Mittlefehldt et al. 1998; Mayne et al. 2009; Mittlefehldt 2015). NWA 8562 has 45 vol% pyroxene ($En_{52-15}Wo_{8-33}Fs_{40-52}$: Fig. 2), 40 vol% plagioclase (An_{89-92}), 10 vol% silica, and 3 vol% olivine (Fa_{83-89}), with accessory troilite, chromite, ilmenite, and ülvospinel. The pyroxenes are strongly zoned with respect to major element concentrations, with a range of compositions from $Fs_{41}Wo_9$ to $Fs_{52}Wo_{33}$ (Fig. 2). The pyroxene zonation follows a normal zoning profile with Fe increasing from core to rim. The major element zoning in NWA 8562 pyroxene is consistent with MG unequilibrated (type 1) eucrites that have not undergone thermal metamorphism (Takeda and Graham 1991; Mayne et al. 2009). Trace element concentrations on pyroxene and plagioclase are available in Tables S1 and S2, respectively, in supporting information.

Fe-enrichment along pyroxene rims, as found here in NWA 8562, has been interpreted to be a by-product of secondary metasomatism in other eucrites (Mittlefehldt and Lindstrom 1997; Schwartz and McCallum 2005; Barrat et al. 2011; Zhang et al. 2013; Warren et al. 2014; Mayne et al. 2016), but could also have formed by late-stage igneous processes.

The bulk compositional data for NWA 8562 are also consistent with this eucrite being a normal member of the MG eucrites. Bulk trace element compositions for NWA 8562 are consistent with MG eucrites, La (2.5 μg g^{-1}) and FeO_T/MgO (3.26) (Table 1), exhibiting a flat CI-normalized REE pattern at about 12× chondritic (Fig. 3). Additional data from the trace element analyses for determination of the bulk composition are available in Table S3 in supporting
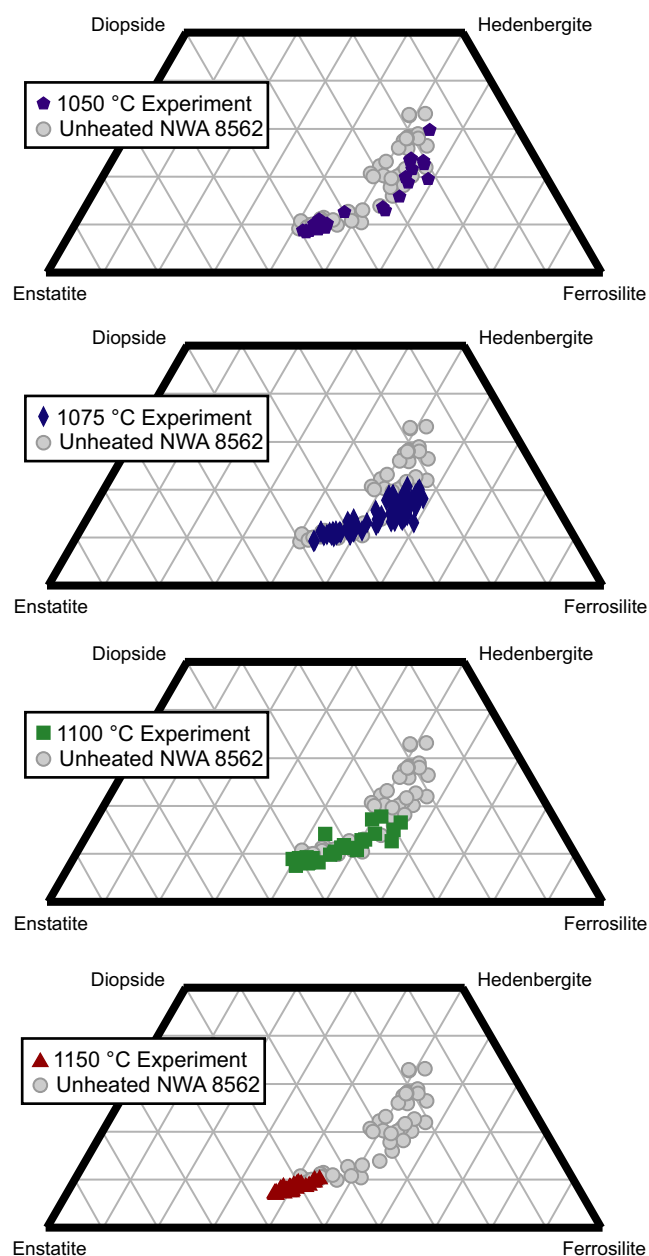

Fig. 2. Composition of pyroxene in experimental charges. All quadrilaterals include the pyroxene from unheated starting material (NWA 8562) for reference. Pyroxene compositions across the suite of experiments are consistent with congruent (disequilibrium) melting of pyroxene. (Color figure can be viewed at wileyonlinelibrary.com.)

information. Oxygen isotopic analysis of two replicates gave the following composition for NWA 8562: $\delta^{17}O = 1.768 \pm 0.042‰$, $\delta^{18}O = 3.842 \pm 0.072‰$, $\Delta^{17}O = -0.246 \pm 0.004‰$ (1σ). The $\Delta^{17}O$ composition of NWA 8562 is within error of the mean HED value determined by Greenwood et al. (2005, 2006, 2016) and indicates that NWA 8562 is an isotopically normal member of the HED group.

Table 1. Major element composition of experimental melts. Values below the limits of detection are noted as bdl, and values not measured are noted as n.d.

|	1050 °C 24 h Experiment		1075 °C 48 h Experiment		1100 °C 24 h Experiment		1150 °C 24 h Experiment		1200 °C 24 h Experiment		Yamaguchi et al. (2013) 1070 °C		1100 °C	
n	5		70		42		60		40		4		5	
Spot size	5		1		5		5		5					
	Average	1σ	Average	1σ	Average	1σ	Average	1σ	Average	1σ	Average	1σ	Average	1σ
SiO_2	43.0	0.74	45.3	0.79	48.4	0.70	48.6	0.82	48.5	0.50	50.3	0.5	50.6	0.3
TiO_2	4.62	0.08	2.70	0.25	1.63	0.20	0.89	0.05	0.66	0.04	1.78	0.19	2.06	0.08
Al_2O_3	7.19	0.29	8.66	0.48	9.46	0.31	11.34	0.27	13.18	0.21	15.5	1.9	10.2	0.1
Cr_2O_3	0.05	0.01	0.06	0.02	0.12	0.01	0.18	0.06	0.20	0.05	0.2	0.2	0.12	0.03
FeO	31.3	1.36	28.0	0.81	25.6	0.90	22.3	0.93	20.2	0.18	16.8	1.8	21.1	0.3
MnO	0.67	0.01	0.70	0.07	0.59	0.04	0.56	0.04	0.51	0.02	0.42	0.1	0.59	0.07
MgO	1.68	0.02	1.80	0.16	2.86	0.10	4.94	0.16	6.51	0.08	1.78	0.22	3.2	0.07
NiO	bdl		bdl		bdl		bdl		bdl		n.d.		n.d.	
CaO	9.50	0.36	9.65	0.18	9.94	0.14	10.0	0.21	9.85	0.07	11.8	0.5	10.8	0.1
Na_2O	0.26	0.08	0.59	0.07	0.37	0.08	0.39	0.08	0.34	0.06	0.79	0.9	0.69	0.05
K_2O	0.12	0.02	0.06	0.01	0.04	0.02	0.03	0.02	0.03	0.02	0.25	0.3	0.12	0.01
P_2O_5	0.60	0.13	0.24	0.13	0.13	0.03	0.08	0.01	0.06	0.02	0.38	0.7	0.23	0.06
SO_3	0.73	0.46	n.d.		0.35	0.21	0.20	0.06	0.12	0.01	n.d.		n.d.	
Total	99.67	0.49	97.78	0.62	99.52	0.82	99.54	1.93	100.11	0.70	100.0		99.71	
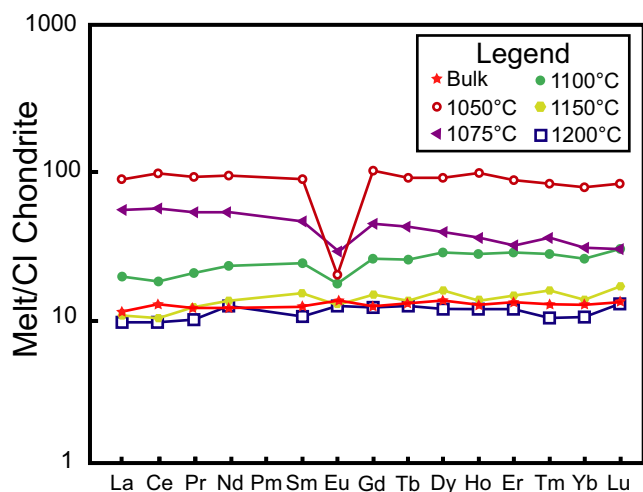
Fig. 3. Rare earth element concentrations of experimental melts and bulk NWA 8562. Trace element concentrations are normalized to CI chondrite determination of Anders and Grevesse (1989). Melts generated in lower temperature experiments are more enriched in REE elements, with the exception of Eu. The 1075 °C experimental melt is the only melt that is slightly enriched in LREE, which may reflect a greater contribution of phosphates to melt at this temperature. The similarity between the melt composition at 1150 °C to the bulk composition indicates that at this temperature the phases with greater than bulk trace element concentrations have melted. (Color figure can be viewed at wileyonlinelibrary.com.)

Characterization of Experimental Products

1050 °C Experiment

The 1050 °C, IW-0.5, 24 h run yielded a melt fraction of ~5 vol% based on modal analysis. These melt pockets (<20 μm diameter) occur exclusively within mesostasis-rich regions of silica laths, subhedral ilmenite, ülvospinel, and fayalite (Fig. 1b). Frequently melt pools track plagioclase–pyroxene grain interfaces straddling silica laths in these mesostasis-rich areas. In this experimental charge, five melt pools large enough to analyze by EMP (>5 μm) were found, but only one was large enough to analyze by LA-ICP-MS (>15 μm). The major and minor element compositions varied only moderately between the five melt pools (1σ standard deviation for FeO is 1.36 wt%; Table 1) analyzed by EMP. Melt occasionally forms thin short veins (≤2 μm in width and 10–30 μm in length) that may be following pre-existing fractures, particularly in plagioclase. Mesostasis areas, including oxides, sulfides, olivine, and silica, are often adjacent to or surrounded by melt, suggesting incomplete melting of these phases. Pyroxenes retain Fe-Mg zonation, with the most magnesian compositions similar to the unheated material ($Fs_{42}Wo_9$) with the most calcic end of the trend at $Fs_{54}Wo_{30}$, slightly below the unheated NWA 8562 (Fig. 2). Relative to bulk NWA 8562, the melt is enriched in FeO and depleted in MgO, Al_2O_3, and SiO_2 (Fig. 4). The average FeO/MgO ratio of the melts is 18.6 (Table 1). The melts are also strongly enriched in TiO_2 and P_2O_5, which are both relatively incompatible in eucrites (Barrat et al. 2007). Trace element concentrations for the 1050 °C melt could only be determined for one melt pocket due to the small size of most melt pockets in this charge. The melt exhibits a moderate negative Eu anomaly (Fig. 3). The melt fraction is enriched in incompatible trace elements (e.g.,
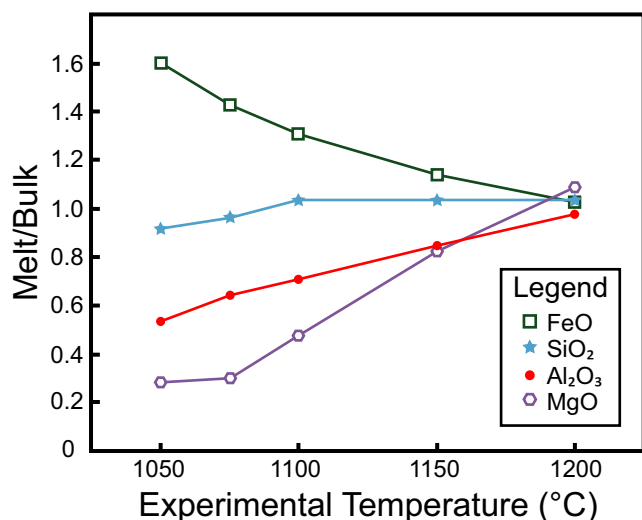
Fig. 4. Major element variation diagram. Experimental melt compositions are normalized to bulk NWA 8562, as determined by LA-ICP-MS. As experimental temperatures increase, melt compositions become less depleted in MgO, Al_2O_3, and SiO_2 and less enriched in FeO relative to bulk NWA 8562. The 1200 °C melt composition is within analytical uncertainties of bulk NWA 8562 for these elements. (Color figure can be viewed at wileyonlinelibrary.com.)

REE; Table 1) relative to bulk NWA 8562. Excluding Eu, this melt has roughly seven to nine times higher concentrations of REE than in the bulk NWA 8562 and about three to five times higher concentrations of REE than the 1100 °C experimental melt product (Table 1). The highly incompatible elements Hf, Ta, and Th yield a melt fraction of 6–9%, slightly higher but within the uncertainty of the analysis.

1075 °C Experiment

The 1075 °C, IW-0.5, 48 h run yielded a melt fraction of ~8 vol% from modal analysis. Mesostasis areas have largely been melted, aside from sparse, small cores of relict silica and ilmenite. These melt zones are usually located at pyroxene–plagioclase grain boundaries, frequently enclose silica laths, and are typically 10–100 μm in width and 80–300 μm in length (Fig. 1c). Melt occasionally forms thin, elongate veins (4–10 μm in width and 150–500 μm in length) that may be following pre-existing fractures. In this experimental charge, eight melt pools large enough to analyze by EMP (>5 μm) were found, and four large enough to analyze by LA-ICP-MS (>15 μm). The variation in major element concentrations is within the analytical uncertainties of the EMP analyses, and the 1σ standard deviation in La concentrations between melt pools is ~8% of the average (Table 2). Iron-rich rims of pyroxene have been extensively melted, leaving cores with central magnesian compositions ($Fs_{43}Wo_9$) and rims considerably less calcic ($Fs_{55}Wo_{21}$)

than unheated NWA 8562 (Fig. 2). The melt shows an FeO enrichment (Fig. 4) and is depleted in MgO, Al_2O_3, and SiO_2 relative to bulk NWA 8562, but to a smaller extent than melt in the 1050 °C experiment. The average FeO/MgO ratio of the melts is 15.6 (Table 1). The melt exhibits a slightly LREE-enriched pattern at two to five times chondritic abundances, with a moderate negative Eu anomaly (Fig. 3). The highly incompatible elements Hf, Ta, and Th yield a melt fraction of 14–19%, higher than the modal analysis.

1100 °C Experiment

The 1100 °C at IW-0.5 24 h run experiment yielded a melt fraction of ~18 vol% by modal analysis. No mesostasis areas are present at this temperature. Melt occurs at all pyroxene–plagioclase grain boundaries as 25–50 μm wide zones that frequently embay both phases (Fig. 1d). Silica laths (10–50 μm in their longest direction), which likely are residual and occur at the original pyroxene–plagioclase grain boundaries, are commonly enclosed in the center of the melt, suggesting melting of both pyroxene and plagioclase. Partial melting of Fe-rich pyroxene has occurred, producing a range of compositions similar to the 1075 °C experiment ($Fs_{40}Wo_9$–$Fs_{55}Wo_{15}$) (Fig. 2). Major elements in the melt show similar but less pronounced enrichment in FeO and depletions in MgO and Al_2O_3 when compared to the lower temperature melts (1050 and 1075 °C). The FeO/MgO ratio of the melt is 8.95 (Table 1). The melt has comparable SiO_2 concentration to bulk NWA 8562 (Fig. 4). REEs are slightly enriched at 1.4–2.4 times chondritic, with a slight HREE enrichment indicative of preferential melting of pyroxene relative to plagioclase and a slight negative Eu anomaly (Fig. 3). The highly incompatible elements Hf, Ta, and Th yield a melt fraction of 36–50%, which is two to three times higher than the modal analysis.

1150 °C Experiment

The experimental run at 1150 °C, IW-0.5 for 24 h produced extensive melting (52 vol% melt by modal analysis). The chip retained its original shape in general; however, melt wetted one corner of the chip onto its container. This is the lowest temperature step at which melt macroscopically wicked out of the chip onto the alumina crucible containing it. Large melt pools (e.g., 300×300 μm) formed in this charge (Fig. 1e). At this temperature, pyroxene is only extant as pervasively embayed agglomerations of relict Mg-rich cores (Fig 2). Plagioclase rim regions have been consumed by melting, but plagioclase grains are not as extensively embayed as the pyroxene in these experimental charges. Major elements in the melt exhibit a slight enrichment in FeO and small depletions in MgO and Al_2O_3 relative to bulk

Table 2. Composition of experimental melts and bulk NWA 8562. Concentrations of oxides are in wt% and trace elements are in µg g⁻¹. Values below the limits of detection are noted as bdl, and values not measured are noted as n.d.

	Bulk NWA 8562	Experimental melt products				
		1050 °C	1075 °C	1100 °C	1150 °C	1200 °C
n		1	4	10	5	4
SiO_2	46.9	42.9	45.1	48.4	48.5	48.4
TiO_2	0.66	4.62	2.71	1.63	0.89	0.66
P_2O_5	0.05	0.6	0.23	0.13	0.08	0.06
Al_2O_3	13.4	7.19	8.65	9.46	11.3	13.1
Cr_2O_3	n.d.	0.05	0.06	0.12	0.18	bdl
FeO	19.5	31.2	27.9	25.6	22.3	20.1
MnO	0.59	0.67	0.71	0.59	0.56	0.51
MgO	5.99	1.68	1.79	2.86	4.94	6.51
NiO	n.d.	bdl	0.01	bdl	bdl	bdl
CaO	12.1	9.50	9.64	9.94	10.0	9.85
Na_2O	0.5	0.26	0.58	0.37	0.39	0.34
K_2O	0.05	0.12	0.06	bdl	bdl	0.03
FeO/ MgO	3.26	18.6	15.6	8.95	4.51	3.09
Sc	n.d.	45	41	n.d.	n.d.	bdl
Rb	0.5	<11.70	<2.1	0.33	bdl	0.33
Sr	97	107	89.9	78	61	15
Y	19	124	82.8	31	19	15
Zr	44	399	231	71	44	36
Nb	2.6	n.d.	n.d.	4.3	2.8	2.2
Ba	45	178	122	60	34	34
La	2.5	21	12.9	4.5	2.4	2.2
Ce	7.4	59	34	10.6	5.9	5.5
Pr	1.0	8.2	4.75	1.8	1.0	0.9
Nd	5.1	43	24	10.1	5.9	5.5
Sm	1.7	13	6.7	3.4	2.2	1.5
Eu	0.72	1.1	1.56	0.96	0.68	0.68
Gd	2.3	20	8.6	5.0	2.8	2.3
Tb	0.46	3.3	1.51	0.90	0.47	0.44
Dy	3.2	22	9.4	6.7	3.7	2.8
Ho	0.68	5.4	1.9	1.5	0.7	0.6
Er	2.0	14	5	4.45	2.24	1.83
Tm	0.30	2	0.85	0.66	0.36	0.24
Yb	2.0	13	4.9	4.1	2.1	1.6
Lu	0.31	2	0.71	0.73	0.40	0.30
Hf	1.3	19	7.1	2.6	1.5	1.2
Ta	0.13	2.3	0.94	0.36	0.19	0.13
Th	0.27	3.0	1.4	0.56	0.33	0.29
U	0.09	1.0	0.38	0.18	0.09	0.07

NWA 8562 (Fig. 4). As in the 1100 °C experiments, the melt has comparable SiO_2 concentration to bulk NWA 8562. The REE concentrations of the melt product in this run are similar to those of bulk NWA 8562, which implies that the pyroxene–plagioclase ratio entering the melt has approximately the same value as bulk NWA 8562. The highly incompatible elements Hf, Ta, and Th

yield a melt fraction of 68–87%, which is 1.5 times higher than the modal analysis.

1200 °C Experiment

Nearly complete melting occurred in the 1200 °C at IW-0.5 24 h run experiment. The experimental melt pooled at the bottom of the alumina crucible and formed a meniscus; the original shape of the chip was not preserved (Fig. 1f). In this experiment, the melt fraction is 97 vol% with only a few small grains of plagioclase, Mg-rich pyroxene, and chromite remaining. Due to the extent of melting in this experiment, the major element composition of the melt fraction is nearly equal to that of bulk NWA 8562 (Fig. 4). The equivalent Al_2O_3 concentration of this melt compared to bulk NWA 8562 (respectively, 13.1 and 13.4 wt% Al_2O_3; Table 1) suggests that even with near-complete melting and pooling of the melt in the alumina (Al_2O_3 ceramic) crucible, the melt did not react with its refractory container. Lower Na_2O concentrations in the 1200 °C compared to the unheated NWA 8562 bulk composition (respectively, 0.34–0.50 wt% Na_2O; Table 1) can be attributed to loss of this volatile element during these experiments. The trace element concentrations of the melt product are also consistent with the bulk composition of NWA 8562 determined by LA-ICP-MS of the unheated sample (Fig. 3).

DISCUSSION

Approach to Equilibrium

While our experimental conditions (24–48 h) were comparable to previous eucrite partial melting experiments (Stolper 1977; Yamaguchi et al. 2013), these relatively short run times limit the attainment of equilibrium. We evaluate our approach to equilibrium by comparing compositional variations between melt pools, modal and chemical indicators of the melt fraction, calculating mineral–melt distribution coefficients, and examining zoning within residual pyroxene.

A first-order assessment of equilibrium in partial melting experiments on natural samples is to consider variations between separate melt areas within an experimental charge. For the 1050 °C experiment, there was only one melt pool large enough to analyze for trace elements, which raises concern that this measurement might not be representative. However, there is little variation in the major and minor element composition of the five melt pools measured by EMP analysis (Table 1). If localized grain boundary conditions around the melt pools predominately controlled melt composition, we would expect greater variation between melt pools, as observed in endmember disequilibrium melting (e.g.,

Lunning et al. 2017). The major and minor element variations between melt in the experiments at 1075–1200 °C are also within the uncertainties of EMP analyses, which indicates the melt in these experiments is homogeneous in composition, and this is reflected in the trace element abundance variations. Modal analyses of melt fraction exhibit significant differences with melt fractions calculated from the distribution of highly incompatible elements Hf, Ta, and Th. While the modal abundance of melt is within analytical uncertainty from the LA-ICP-MS analyses at 1050 °C (~5 versus 6–9 vol%), they differ outside the range of uncertainty by factors of 1.5–3 at 1075–1150 °C. This may reflect disequilibrium inherited from the starting material. Further evidence for disequilibrium at 1100 and 1150 °C is provided by FeO/MgO distribution coefficients (K_D) between pigeonite and melt. Equilibrium eucrite crystallization experiments at 1 bar pressure at 1150 °C with coexisting glass, olivine, pigeonite, plagioclase, and spinel for two eucritic compositions (Bartels and Grove 1991) yielded K_D of 0.26–0.27. Mineral–melt partition coefficients for our most evolved pyroxene composition (Fig. 2) compared to the coexisting average melt (Table 1) yields similar K_D values at 1050 and 1075 °C, but measured K_D values at 1100 (0.39) and 1150 °C (0.36) differ substantially. This trend of apparently greater disequilibrium in the higher temperature partial melting experiments is counterintuitive for experiments of the same duration, which would typically more effectively approach equilibrium at higher temperatures. This could reflect that residual pyroxenes at higher temperatures are just the cores of the original zoned grains, which did not originally crystallize at equilibrium and would have to undergo extensive subsolidus diffusion to come to equilibrium with our experimental melts. K_D differences could be more pronounced at greater degrees of melting because the experimental melting did not follow a hysteresis path with the natural cooling of the starting material. Differences in cooling/melting paths may have been less pronounced at lower degrees of melting. The composition of the residual pyroxene across the experimental temperature series (Fig. 2) illustrates that in the higher temperature experiments, only the Mg-rich pyroxene cores remain. It is notable that the residual pyroxene in the 48 h (1075 °C) experiment does not extend to as Mg-rich compositions as in all of the 24 h experiments (Fig. 2c compared to Figs. 2a, 2b, and 2d).

Pyroxene zoning is present in all of the residual pyroxenes from 1050 to 1150 °C, with the ranges in the zoning extending to less calcic at higher experimental temperatures (Fig. 2). Homogenization of these residual pyroxene grains via lattice diffusion at length scales of 15 μm and a temperature of 1050 °C would require calculated run times of ~100 days using diffusion rates for

pyroxene that are ~10^3 lower (Huebner and Nord 1981) than measured for olivine (Buening and Buseck 1973).

The duration of partial melting and melt assimilation envisioned by Barrat et al. (2007) could depend on a number of factors including the time scale of wall rock melting, migration of that melt, and movement of the assimilating magma through the crust. Given the impracticality of such long experimental run times, one alternative approach might be to use an equilibrated eucrite as the starting material, as was done by Yamaguchi et al. (2013), to achieve major element equilibrium. The lower temperature experiments in our study and in those of Yamaguchi et al. (2013) are quite different, and some of this can be attributed to different experimental setups. The unequilibrated nature of our starting material, in which pyroxene exhibits major element zoning with Mg-rich cores grading to Fe-rich rims, may have produced a melt with higher FeO/MgO ratios than would form from an otherwise similar equilibrated eucrite. Therefore, the FeO concentrations from our experimental melt represent an upper bound for eucritic crustal partial melts. In contrast, Yamaguchi et al. (2013) reported that FeO-rich olivine crystallized in their experiments upon quenching and that their experiments lost Fe to the Pt crucible, both of which would have lowered the FeO concentration of the remaining melt; thus the FeO concentrations from the Yamaguchi et al. (2013) experiments represent a lower bound for eucritic crustal partial melts.

Equilibrium with regard to certain trace elements (i.e., Hf, Ta, Th, REE) take longer to approach than for the major elements focused on in this work (i.e., Mg, Fe) in partial melting experiments. Feldstein et al. (2001) demonstrated that in partial melting experiments using an equilibrated chondrite (Leedey, L6) as the starting material, REE concentrations in partial melts from experiments run for 1 h and 3 days were respectively ~3–5 times and ~2 times lower than in experiments run for 3 weeks. Both our experiments and those of Yamaguchi et al. (2013) were only run for 24–48 h, which is not long enough to closely approach equilibrium with regard to REE. As with the experiments of Feldstein et al. (2001), REE concentrations in the melt would increase given more time to approach equilibrium. With this caveat regarding REE equilibrium in mind, we can use the REE concentrations from our experimental melts as lower bounds on the concentrations expected for eucritic crustal melts.

Testing Stannern-Trend Petrogenesis by Assimilation of Crustal Partial Melts

Melting of NWA 8562 at 1050–1100 °C produced melts rich in incompatible elements (e.g., TiO_2, FeO, REE). These results are similar to those of Stolper (1977)

for major element compositions and Yamaguchi et al. (2013) for trace elements. Stolper (1977) found higher concentrations of FeO and TiO_2 in eucrite partial melts generated at progressively lower temperatures in their experiments, down to 1108 °C at IW-0.6. The melt produced in the 1100 °C at IW-1 experiment by Yamaguchi et al. (2013) contained REE concentrations four to five times higher than their starting material, HaH 262, with a pronounced negative Eu anomaly. The coordinated major, minor, and trace element compositions measured in our experimental melts can be used to test, for both incompatible and major elements, whether contamination by these crustal melts into MGNL-trend magmas could produce Stannern-trend magmas (Barrat et al. 2007).

Barrat et al. (2007) showed that simple binary mixing calculations yielded comparable results to the assimilation and fractional crystallization (AFC) equations from DePaolo (1981) to effectively model the partial melt contamination scenario for the petrogenesis of Stannern-trend eucrites. The same binary mixing calculations are employed below to model both trace and major elements for mixing of MGNL magmas and crustal partial melts. The resulting mixture compositions can be defined by:

$$C_m = (C_a * f) + (C_o * [1 - f]) \qquad (1)$$

where C_m is the concentration of an element in the resultant magma mixture, C_a is the concentration of the assimilating component (i.e., partial melt), C_o is the concentration of the uncontaminated magma, and f is the proportion of the assimilating component in the magma mixture.

Barrat et al. (2007) demonstrated that addition of 5–15% partial melts ($f = 0.05$–0.15) calculated for a typical MGNL eucrite, Juvinas, added to a bulk Juvinas-composition can reproduce the entire Stannern-trend with respect to trace elements. A similar conclusion can be reached when applied to the experimental results of Yamaguchi et al. (2013), where mixing of 5–15% melt experimentally produced at 1100 °C from the equilibrated eucrite HaH 262 to the bulk composition of that meteorite produces trace element compositions within the range of Stannern-trend eucrites. Neither of these models considered how the major element compositions would behave with the addition of this crustal partial melt.

Contaminated Eucrite-Composition Magmas

In order to evaluate the effect on major, minor, and trace element composition of assimilation of a crustal partial melt, we modeled eucrite-composition magmas contaminated by varying proportions (5–15%) of our lowest-degree partial melts (Table 2). We modeled eucritic magmas with the composition of our starting material NWA 8562 and Juvinas. Additions of 5–15% crustal partial melts bring La concentrations of the contaminated eucritic magmas into the range of La concentrations for known Stannern-trend eucrites (Fig. 5a), just as is observed for both Juvinas (Barrat et al. 2007) and HaH 262 (Yamaguchi et al. 2013).

The contaminated NWA 8562 magma has a simultaneous increase in FeO/MgO values away from known Stannern-trend eucrites (Fig. 5a), a factor that previous models and experiments did not address. Bulk data for Stannern-trend eucrites indicate that whichever mechanism is evoked for their petrogenesis, there must be an increase in incompatible trace elements, with only minimal change in FeO/MgO. A NWA 8562-composition cannot produce known Stannern-trend magmas, unless the crustal partial melt was both trace element enriched and had a much lower FeO/MgO ratio than NWA 8562, which neither our experimental data nor Yamaguchi et al.'s (2013) data support. It is important to consider the possibility that the composition of NWA 8562 is too evolved (i.e., too Fe-rich) to be contaminated to produce the Stannern-trend, as it has a bulk FeO/MgO value of 3.3, compared to 2.6 for Juvinas and 3.1 for HaH 262. Therefore, we assess the possibility that the magma being contaminated is more primitive (more Mg-rich) than NWA 8562.

Juvinas has been proposed as close to a primary magma for the entire MGNL-trend eucrites (Stolper 1977; Pun and Papike 1996) and, as mentioned above, is among the more Mg-rich of the MGNL-trend eucrites. Although cumulate eucrites are more Mg-rich than Juvinas, their bulk compositions cannot be treated as magma compositions because, inherently, they contain evidence for crystal accumulation; they are not suitable compositions to consider here. We modeled a Juvinas-composition magma contaminated by varying proportions (5–15%) of our lowest-degree crustal partial melts (Table 2; Fig. 5b). The binary mixing model using our experimental melt composition yields minor and trace element concentrations, e.g., Ti and La, consistent with those of most Stannern-trend eucrites but does not extend to the most trace element-enriched Stannern-trend eucrites (Figs. 5 and 6). Juvinas-composition magmas contaminated with 1050 and 1075 °C experimental melts reproduce Stannern-trend eucrite compositions with respect to Ti and FeO/MgO (Fig. 6), the minor and major elements initially used to define the Stannern-trend eucrites (Stolper 1977). However, these contaminated magmas only skirt the Stannern-trend eucrites in FeO/MgO versus La space (Fig. 5b). The major element mixing trend suggests that Stannern-trend eucrites had to form by contamination of a Juvinas-like primary magma. This finding is

supported by the primitive chlorine isotope signature of Stannern, which coincides with those of the less evolved MG eucrites (Sarafian et al. 2017).

Equilibrium Crustal Partial Melting on the HED Parent Body

The petrogenesis of Stannern-trend eucrites by assimilation of crustal partial melts works, if the crustal partial melts form under equilibrium conditions with regard to major, minor, and trace elements. Barrat et al. (2007) modeled that 5% equilibrium partial melting of Juvinas-composition eucrite would generate a partial melt with 41 ppm La, which is about twice the abundance of La in our 1050 °C experiment which formed ~5% melt. As discussed previously, although 24 h duration experiments enabled us to determine an upper bound on the FeO concentration in partial melts from eucritic crustal material, our experiments did not, with respect to REE, closely approach equilibrium. REE concentrations in partial melts in our experiments, and those of Yamaguchi et al. (2013), were lower than if the experiments had been run for longer to approach trace element equilibrium, based on the experimental time series study by Feldstein et al. (2001). To produce all the Stannern-trend eucrites, crustal partial melts need to be more enriched in trace elements relative to FeO than experimentally generated in this work. If the trace element abundances modeled by Barrat et al. (2007) for eucritic partial melts are combined with major element data from our experiments with similar percentage of partial melting, the major and trace element compositional trend of the Stannern-trend eucrites can be reproduced (Fig. 7). Additional experiments to investigate the evolution of trace element concentrations relative to experimental duration are needed to fully explore this hypothesis. Equilibrium partial melting of a metamorphosed eucritic lower crust on the HED parent body, as hypothesized by Barrat et al. (2007), is consistent with partial melts approaching trace element equilibrium. This equilibrium crustal partial melting is also consistent with the formation of trace element-depleted residual eucrites that resemble MG eucrites with regard to major element concentrations (Yamaguchi et al. 2009), magmas formed entirely of crustal partial melt, as suggested by Hahn et al. (2017), and evidence that some diogenite parental melts may have been contaminated by crustal partial melts (Barrat et al. 2010).

Equilibrium crustal partial melting is notable, because other early solar system igneous lithologies formed by low degrees of partial melting exhibit trace element trends (Benedix et al. 2000; Feldstein et al. 2001; Day et al. 2012; Bischoff et al. 2014) and sometimes even major element concentrations (Lunning
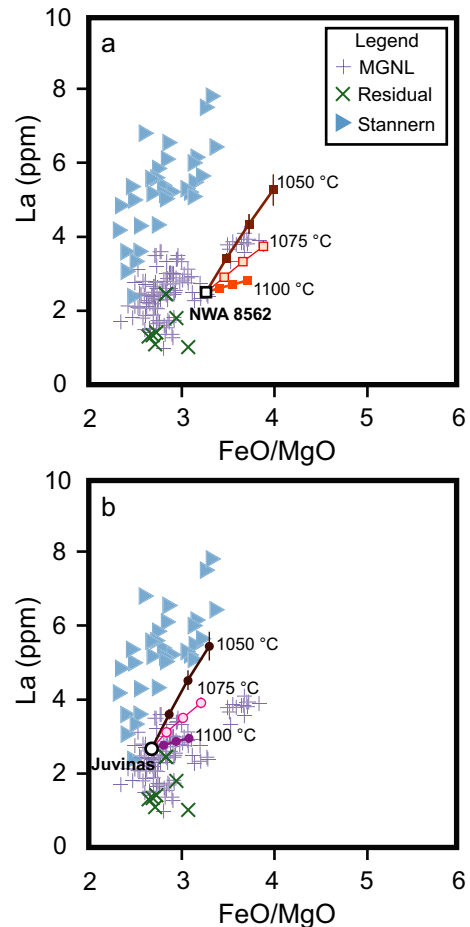

Fig. 5. Magma contamination La versus FeO/MgO variation diagrams. Analytical errors on MgO and FeO when propagated through the model calculation are within areas of the symbols. Analytical errors on La are displayed as error bars when they extend beyond the areas of the symbols. The major element compositional variation between melt pools is within EMP analytical errors for experiments at 1075 and 1100 °C. The melt pools from the 1050 °C experiment exhibit compositional variation in FeO (Table 1); however, when this variation is propagated it falls within the area of the data symbols. a) La versus FeO/MgO plot showing a bulk NWA 8562 composition contaminated by the melts produced for each experiment in this study. Each line shows the compositional change from the measured bulk composition for NWA 8562, through contamination with 5%, 10%, and 15% melt, respectively, for each temperature. b) La versus FeO/MgO plot showing a bulk Juvinas-composition contaminated by the melts produced for each experiment in this study. Each set of symbols shows the compositional change from bulk Juvinas, through contamination with 5%, 10%, and 15% melt, respectively.

et al. 2017) consistent with disequilibrium melting. The evidence presented here that Stannern-trend eucrite formation by equilibrium partial melting of the eucritic crust highlights the complexity of the petrology of the
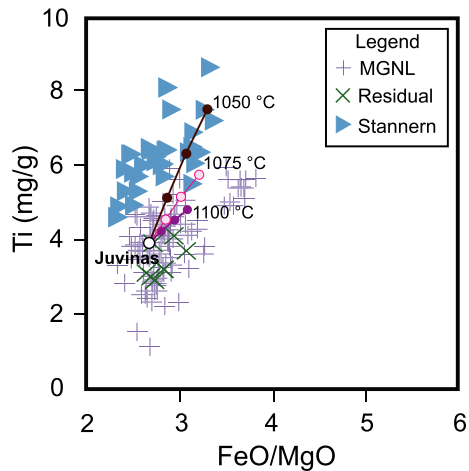
Fig. 6. Ti versus FeO/MgO variation diagram showing a Juvinas-composition magma contaminated by the melts produced for each experiment in this study. Analytical errors on Ti, MgO, and FeO when propagated through the model calculation are within the area of the symbols. Each set of symbols shows the compositional change from bulk Juvinas, through contamination with 5%, 10%, and 15% melt, respectively.

HED parent body and the diversity of magmatic processes in the early solar system.

The one aspect of the Stannern-trend eucrite suite that we cannot fully explain with the model of Barrat et al. (2007) are the members with FeO/MgO ratios comparable or more Mg-rich than eucritic primary magmas (e.g., Juvinas). Contamination by our or Yamaguchi et al.'s (2013) crustal partial melts would form magmas with slightly higher FeO/MgO ratios than the primary magma prior to contamination (Fig. 6). The formation of Stannern-trend members with low FeO/MgO ratios must require a subsequent process to reduce their Fe concentrations or increase their Mg concentrations; future studies are needed to explain the complete petrogenesis of these members of the Stannern-trend.

CONCLUSIONS

Low degrees of experimental partial melting of a Main Group/Nuevo Laredo-trend eucrite generated melt enriched in FeO, TiO_2, P_2O_5, and REE and depleted in Al_2O_3, SiO_2, and MgO. The compositions of the lowest-degree partial melts, formed by ~5% experimental melting of NWA 8562 at 1050 °C and IW-0.5, are compositional analogs for the crustal partial melts proposed by Barrat et al. (2007) that contaminate MGNL-trend eucritic magmas to form Stannern-trend eucritic magmas. We used binary mixing models to test if assimilation of crustal partial melts by MGNL-trend
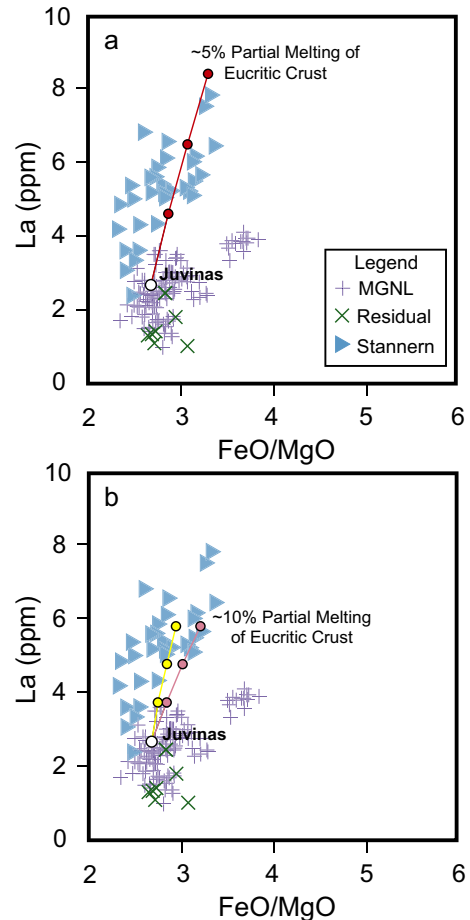

Fig. 7. Magma contamination variation diagram combining trace element modeling by Barrat et al. (2007) with major element determinations from our experiments. La versus FeO/MgO plots showing a Juvinas-composition magma contaminated by eucritic crustal partial melts. The partial melt compositions in this plot use the La concentrations modeled by Barrat et al. (2007). Each set of circles tracks the compositional change from bulk Juvinas, through contamination with 5%, 10%, and 15% melt, respectively. a) The red circles are from binary mixing models using the major element concentrations of the melt in our 1050 °C experiment (5% melt, modally) and the La concentrations modeled by Barrat et al. (2007) for 5% crustal partial melts. b) Both sets of data (yellow and pink circles) are from binary mixing models using the La concentrations modeled by Barrat et al. (2007) for 10% crustal partial melts, the models for pink (right) set of circles included major element concentrations from our 1075 °C experiment (8% melt, modally), and the yellow (left) set of circles included major element concentrations from the melt of the Yamaguchi et al. (2013) 1070 °C experiment. This plot demonstrates that contamination of a Juvinas-composition magma with low-degree crustal partial melts can explain both the trace element and the major element abundance patterns of the Stannern-trend eucrites.

magmas could produce Stannern-trend magmas. To simultaneously produce the trace, minor, and major element abundances of the Stannern-trend eucrites, the crustal partial melts need to form by equilibrium partial

melting of the eucritic crust and the magma being contaminated needs to be a primary eucritic magma (e.g., Juvinas-composition magma).

Editorial Handling—Dr. Kevin Righter

REFERENCES

Anders E. and Grevesse N. 1989. Abundances of the elements: Meteoritic and solar. *Geochimica et Cosmochimica Acta* 53:197–214.

Barrat J. A., Blichert-Toft J., Gillet P., and Keller F. 2000. The differentiation of eucrites: The role of in situ crystallization. *Meteoritics & Planetary Science* 35:1087–1100.

Barrat J. A., Yamaguchi A., Greenwood R. C., Bohn M., Cotten J., Benoit M., and Franchi I. A. 2007. The Stannern trend eucrites: Contamination of main group eucritic magmas by crustal partial melts. *Geochimica et Cosmochimica Acta* 71:4108–4124.

Barrat J. A., Yamaguchi A., Greenwood R. C., Benoit M., Cotten J., Bohn M., and Franchi I. A. 2008. Geochemistry of diogenites; still more diversity in their parental melts. *Meteoritics & Planetary Science* 43:1759–1775.

Barrat J. A., Yamaguchi A., Zanda B., Bollinger C., and Bohn M. 2010. Relative chronology of crust formation on asteroid Vesta: Insights from the geochemistry of diogenites. *Geochimica et Cosmochimica Acta* 74:6218–6231.

Barrat J. A., Yamaguchi A., Bunch T. E., Bohn M., Bollinger C., and Ceuleneer G. 2011. Possible fluid-rock interactions on differentiated asteroids recorded in eucritic meteorites. *Geochimica et Cosmochimica Acta* 75:3839–3852.

Barrat J. A., Yamaguchi A., Jambon A., Bollinger C., and Boudouma O. 2012. Low-Mg rock debris in howardites: Evidence for KREEPy lithologies on Vesta? *Geochimica et Cosmochimica Acta* 99:193–205.

Bartels K. S. and Grove T. L. 1991. High-pressure experiments on magnesian eucrite compositions: constraints on magmatic processes in the eucrite parent body. Proceedings, 21st Lunar and Planetary Science Conference. pp. 351–365.

Beck A. W. and McSween H. Y. 2010. Diogenites as polymict breccias composed of orthopyroxenite and harzburgite. *Meteoritics & Planetary Science* 45:850–872.

Beck A. W., Welten K. C., McSween H. Y., Viviano C. E., and Caffee M. W. 2012. Petrologic and textural diversity among the PCA 02 howardite group, one of the largest pieces of the Vestan surface. *Meteoritics & Planetary Science* 47:947–969.

Benedix G. K., McCoy T. J., Keil K., and Love S. G. 2000. A petrologic study of IAB iron meteorites: Constraints on the formation of the IAB-Winonaite parent body. *Meteoritics & Planetary Science* 35:1127–1141.

Bischoff A. and Stöffler D. 1992. Shock metamorphism as a fundamental process in the evolution of planetary bodies: Information from meteorites. *European Journal of Mineralogy* 4:707–755.

Bischoff A., Horstmann M., Barrat J.-A., Chaussidon M., Pack A., Herwartz D., Ward D., Vollmer C., and Decker S. 2014. Trachyandesitc volcanism in the early solar system. *Proceedings of the National Academy of Sciences* 111:12,689–12,692.

Buening D. K. and Buseck P. R. 1973. Fe-Mg lattice diffusion in olivine. *Journal of Geophysical Research* 78:6852–6862.

Day J. M. D., Walker R. J., Ash R. D., Liu Y., Rumble D. III, Irving A. J., Goodrich C. A., Tait K., McDonough W. F., and Taylor L. A. 2012. Origin of felsic achondrites Graves Nunataks 06128 and 06129, and ultramafic brachinites and brachinite-like achondrites by partial melting of volatile-rich primitive parent bodies. *Geochimica et Cosmochimica Acta* 81:94–128.

Delaney J. S., Takeda H., Prinz M., Nehru C. E., and Harlow G. E. 1983. The nomenclature of polymict basaltic achondrites. *Meteoritics & Planetary Science* 18:103–111.

DePaolo D. J. 1981. Trace element and isotopic effects of combined wallrock assimilation and fractional crystallization. *Earth and Planetary Science Letters* 53:189–202.

Duke M. B. and Silver L. T. 1967. Petrology of eucrites, howardites and mesosiderites. *Geochimica et Cosmochimica Acta* 31:1637–1665.

Feldstein S. N., Jones R. H., and Papike J. J. 2001. Disequilibrium partial melting experiments on the Leedey L6 chondrite: Textural controls on melting processes. *Meteoritics & Planetary Science* 36:1421–1441.

Gounelle M., Zolensky M. E., Liou J.-C., Bland P. A., and Alard O. 2003. Mineralogy of carbonaceous chondritic microclasts in howardites: Identification of C2 fossil micrometeorites. *Geochimica et Cosmochimica Acta* 67:507–527.

Greenwood R. C., Franchi I. A., Jambon A., and Buchanan P. C. 2005. Widespread magma oceans on asteroidal bodies in the early solar system. *Nature* 435:916–918.

Greenwood R. C., Franchi I. A., Jambon A., Barrat J.-A., and Burbine T. H. 2006. Oxygen isotope variation in stony-iron meteorites. *Science* 313:1763–1765.

Greenwood R. C., Burbine T. H., Miller M. F., and Franchi I. A. 2016. Melting and differentiation of early-formed asteroids: The perspective from high precision oxygen isotope studies. *Chemie der Erde* 77:1–43.

Hahn T. M., Lunning N. G., McSween H. Y., Bodnar R. J., and Taylor L. A. 2017. Dacite formation on Vesta: Partial melting of the eucritic crust. *Meteoritics & Planetary Science* 52:1173–1196.

Hanson G. N. and Langmuir C. H. 1978. Modeling of major elements in mantle-melt systems using trace element approaches. *Geochimica et Cosmochimica Acta* 42:725–742.

Huebner J. S. and Nord G. L. Jr. 1981. Assessment of diffusion in pyroxenes: What we do and do not know. Proceedings, 12th Lunar and Planetary Science Conference. pp. 479–481.

Humayun M., Davis F. A., and Hirschmann M. M. 2010. Major element analysis of natural silicates by laser

ablation ICP-MS. *Journal of Analytical Atomic Spectrometry* 25:998–1005.

Lunning N. G., McSween H. Y., Tenner T. J., Kita N. K., and Bodnar R. J. 2015. Olivine and pyroxene from the mantle of asteroid 4 Vesta. *Earth and Planetary Science Letters* 418:126–135.

Lunning N. G., Welten K. C., McSween H. Y., Caffee M. W., and Beck A. W. 2016a. Grosvenor Mountains 95 howardite pairing group: Insights into the surface regolith of asteroid 4 Vesta. *Meteoritics & Planetary Science* 51:167–194.

Lunning N. G., Corrigan C. M., McSween H. Y., Tenner T. J., Kita N. K., and Bodnar R. J. 2016b. CV and CM chondrite impact melts. *Geochimica et Cosmochimica Acta* 189:338–358.

Lunning N. G., Gardner-Vandy K. G., Sosa E. S., McCoy T. J., Bullock E. S., and Corrigan C. M. 2017. Partial melting of oxidized planetesimals: An experimental study to test the formation of oligoclase-rich achondrites Graves Nunataks 06128 and 06129. *Geochimica et Cosmochimica Acta* 214:73–85.

Mayne R. G., McSween H. Y. Jr., McCoy T. J., and Gale A. 2009. Petrology of the unbrecciated eucrites. *Geochimica et Cosmochimica Acta* 73:794–819.

Mayne R. G., Smith S. E., and Corrigan C. M. 2016. Hiding in the howardites: Unequilibrated eucrite clasts as a guide to the formation of Vesta's crust. *Meteoritics & Planetary Science* 51:2387–2402.

McCord T. B., Adams J. B., and Johnson T. V. 1970. Asteroid Vesta: Spectral reflectivity and compositional implications. *Science* 168:1445–1447.

McSween H. Y. Jr., Binzel R. P., De Sanctis M. C., Ammannito E., Prettyman T. H., Beck A. W., Reddy V., Corre L., Gaffey M. J., McCord T. B., Raymond C. A., and Russell C. T. 2013. Dawn; the Vesta-HED connection; and the geologic context for eucrites, diogenites, and howardites. *Meteoritics & Planetary Science* 48:2090–2104.

Miller M. F. 2002. Isotopic fractionation and the quantification of ^{17}O anomalies in the oxygen three-isotope system: An appraisal and geochemical significance. *Geochimica et Cosmochimica Acta* 66:1881–1889.

Miller M. F., Franchi I. A., Sexton A. S., and Pillinger C. T. 1999. High-precision d17O isotope measurements of oxygen from silicates and other oxides: Methods and applications. *Rapid Communications in Mass Spectrometry* 13:1211–1217.

Mittlefehldt D. W. 2015. Asteroid (4) Vesta: I. The howardite-eucrite-diogenite (HED) clan of meteorites. *Chemie Der Erde/Geochemistry* 75:155–183.

Mittlefehldt D. W. and Lindstrom M. M. 1993. Geochemistry and petrology of a suite of ten Yamato HED meteorites. *Proceedings of the NIPR Symposium on Antarctic Meteorites* 6:268–292.

Mittlefehldt D. W. and Lindstrom M. M. 1997. Magnesian basalt clasts from the EET92014 and Kapoeta howardites and a discussion of alleged primary magnesian HED basalts. *Geochimica et Cosmochimica Acta* 61:453–462.

Mittlefehldt D. W. and Lindstrom M. M. 2003. Geochemistry of eucrites: Genesis of basaltic eucrites, and Hf and Ta as petrogenetic indicators for altered Antarctic eucrites. *Geochimica et Cosmochimica Acta* 67:1911–1934.

Mittlefehldt D. W., McCoy T. J., Goodrich C. A., and Kracher A. 1998. Non-chondritic meteorites from asteroidal bodies. In *Planetary materials*, edited by Papike J. J. Washington, D.C.: Mineralogical Society of America. pp. 1–195.

Oulton J., Humayun M., Fedkin A., and Grossman L. 2016. Chemical evidence for differentiation, evaporation and re-condensation from silicate clasts in Gujba. *Geochimica et Cosmochimica Acta* 177:254–274.

Pun A. and Papike J. J. 1996. Unequilibrated eucrites and the equilibrated Juvinas eucrite: Pyroxene REE systematics and major, minor, and trace element zoning. *American Mineralogist* 81:1438–1451.

Sarafian A. R., John T., Roszjar J., and Whitehouse M. J. 2017. Chlorine and hydrogen degassing in Vesta's magma ocean. *Earth and Planetary Science Letters* 459:311–319.

Schwartz J. M. and McCallum I. S. 2005. Comparative study of equilibrated and unequilibrated eucrites: Subsolidus thermal histories of Haraiya and Pasamonte. *American Mineralogist* 90:1871–1886.

Shearer C. K., Burger P., and Papike J. J. 2010. Petrogenetic relationships between diogenites and olivine diogenites: Implications for magmatism on the HED parent body. *Geochimica et Cosmochimica Acta* 74:4865–4880.

Stolper E. 1977. Experimental petrology of eucritic meteorites. *Geochimica et Cosmochimica Acta* 41:587–611.

Takeda H. and Graham A. L. 1991. Degree of equilibration of eucritic pyroxenes and thermal metamorphism of the earliest planetary crust. *Meteoritics* 26:129–134.

Warren P. H. and Jerde E. A. 1987. Composition and origin of Nuevo Laredo trend eucrites. *Geochimica et Cosmochimica Acta* 51:713–725.

Warren P. H., Rubin A. E., Isa J., Gessler N., Ahn I., and Choi B. 2014. Northwest Africa 5738: Multistage fluid-driven secondary alteration in an extraordinarily evolved eucrite. *Geochimica et Cosmochimica Acta* 141:199–227.

Yamaguchi A., Taylor G. J., and Keil K. 1996. Global crustal metamorphism of the eucrite parent body. *Icarus* 124:97–112.

Yamaguchi A., Taylor G. J., and Keil K. 1997. Metamorphic history of the eucritic crust of 4 Vesta. *Journal of Geophysical Research* 102:13,381–13,386.

Yamaguchi A., Barrat J. A., Greenwood R. C., Shirai N., Okamoto C., Setoyanagi T., Ebihara M., Franchi I. A., and Bohn M. 2009. Crustal partial melting on Vesta: Evidence from highly metamorphosed eucrites. *Geochimica et Cosmochimica Acta* 73:7162–7182.

Yamaguchi A., Mikouchi T., Ito M., Shirai N., Barrat J. A., Messenger S., and Ebihara M. 2013. Experimental evidence of fast transport of trace elements in planetary basaltic crusts by high temperature metamorphism. *Earth and Planetary Science Letters* 368:101–109.

Yang S., Humayun M., Righter K., Jefferson G., Fields D., and Irving A. J. 2015. Siderophile and chalcophile element abundances in shergottites: Implications for Martian core formation. *Meteoritics & Planetary Science* 50:691–714.

Zhang A., Wang R., Hsu W., and Bartoschewitz R. 2013. Record of S-rich vapors on asteroid 4 Vesta: Sulfurization in the Northwest Africa 2339 eucrite. *Geochimica et Cosmochimica Acta* 109:1–13.

SUPPORTING INFORMATION

Additional supporting information may be found in the online version of this article.

Table S1: LA-ICP-MS of pyroxene in NWA 8562 (unheated). Major and minor elements are listed in wt%. Trace elements are listed in ppm.

Table S2: LA-ICP-MS of plagioclase in unheated NWA 8562.

Table S3: Rastered bulk of NWA 8562 by LA-ICP-MS. Major and minor elements are listed in wt%. Trace elements are listed in ppm.